Self-organized states of quasi-two-dimensional turbulence in an oceanic basin with topography

L. Zavala Sansón

Departamento de Oceanografía Física, Centro de Investigación Científica y de Educación Superior de Ensenada, Carretera Ensenada-Tijuana 3918, Zona Playitas, 22860, Baja California, México.

Received 14 August 2024; accepted 9 December 2024

The evolution of oceanic-scale, quasi-two-dimensional turbulent flows in a closed basin with topography in a rotating system is studied using a shallow-water model. The basin is nearly flat in the central region and has a sloping coastal topography adjacent to the lateral walls. Two problems are analysed for basins in the northern hemisphere (positive Coriolis parameter). The first problem is the slow decay of an initially disordered flow. The main results are (1) the formation of a steady, anticlockwise flow around the basin that follows the topographic contours and (2) the spontaneous generation of an anticyclonic vortex at the nearly flat central part of the domain. This 'preferred' configuration was repeatedly found for arbitrary initial conditions with zero circulation and different Reynolds numbers. The well-defined current around the basin is associated with the direction of propagation of topographic Rossby waves along the contours of constant depth. However, when the initial circulation is sufficiently negative, the resulting flow configuration tends to be anticyclonic over the whole domain, including the coastal regions with topography. The second problem is the evolution of an initial flow at rest that is continuously forced until reaching a quasi-stationary turbulent state. In the presence of random forcing (with no preferential direction in time or space), the flow always tends to the preferred configuration found for decaying flows. The results are discussed in light of recent oceanographic observations in different basins. The limitations of the idealised simulations are outlined, together with recommendations for future studies.

Keywords: Two-dimensional turbulence; topography effects; oceanic vortices.

DOI: https://doi.org/10.31349/RevMexFis.71.030603

1. Introduction

Two-dimensional (2D) turbulence differs remarkably from the three-dimensional (3D) case. In fully developed 2D turbulence, kinetic energy is transferred from small to larger scales in the so-called inverse (or backwards) energy cascade [1], while the opposite occurs in the direct energy cascade of classical 3D turbulence. A consequence for weakly decaying 2D flows (high Reynolds numbers) is that the energy is concentrated in vigorous, large-scale and long-lived vortices, as shown in numerous simulations and demonstrated in several laboratory experiments [2]. An additional ingredient for bounded 2D turbulence in closed domains is the role of lateral boundary conditions [3].

The 2D motion is partially broken when considering fluid layers of finite depth affected by bottom friction, vertical stratification or any other physical condition that entails perpendicular motions [4,5]. However, their effects can be incorporated into quasi-2D formulations when such motions are sufficiently weak. A classic example is bottom friction, often represented by a linear term (Rayleigh friction) in the dynamical equations. A particular case of interest here is the quasi-2D turbulence in rotating flows. Since the early experiments of Taylor [6], it has been known that a homogeneous flow in a constantly rotating system behaves in a quasi-2D fashion: fluid columns remain vertical and parallel to the rotation axis. This behaviour has been thoroughly exploited to study numerous processes in laminar and turbulent flows in rotating tank experiments, which model geophysical flows in the oceans and in the atmosphere [7].

Quasi-2D motions are observed in a rotating system over variable bottom topography, where fluid columns may be squeezed or stretched as they transit from deep to shallow water or vice-versa [8]. The topography can be an isolated feature (*e.g.* a seamount, ridge or basin) or have a random distribution of bumps and valleys. When rotation effects are dominant (low Rossby number), the main characteristic of such systems is that the flow is mainly confined to follow the so-called geostrophic contours f/h, where f is the Coriolis parameter and h the fluid depth (determined by the topography) [9]. For instance, the flow over a submarine mountain in the northern hemisphere ($f > 0$) consists of a clockwise (that is, anticyclonic) flow around the topographic feature. An equivalent result applies in the presence of weakly viscous effects. The primary reason for this behaviour is the material conservation (or nearly conservation when there is viscosity) of potential vorticity, and it has been demonstrated in quasi-geostrophic [10] and shallow-water [11,12] numerical simulations, and in laboratory experiments [13,14].

In particular, we are interested in a bounded ocean basin with sloping topography near the lateral walls. According to the previous description, the flow tends to generate an anticlockwise (cyclonic flow in the northern hemisphere) around the basin and along the topographic slopes. The formation of currents along topographic contours has been discussed previously in several numerical studies of decaying [15-18] and continuously forced [19,20] turbulence. In the presence of random forcing, the currents are generated by the turbulence over the topography, so they appear as the most probable state even in the presence of the forcing [21,22].

Given these antecedents, one may wonder if we should expect that cyclonic circulation is favoured around ocean basins. There are examples suggesting a positive answer. For instance, the so-called Campeche cyclone is frequently formed in the southwestern Gulf of Mexico over the Bahia de Campeche basin [23,24]. However, persistent anticyclonic circulations have also been observed in other locations, such as the Lofoten basin in the Nordic seas [18,25] and other similar basins in the North Atlantic [17]. Thus, a primary question is whether there is any influence of the essential dynamics of the flow-topography interaction described above in the formation of cyclones or anticyclones over oceanic topographic depressions. Does the flow tend towards a 'preferred' state characterised by a dominant vortex and boundary currents? What is the sense of such preferred circulations?

To address these questions from a fundamental point of view, we present numerical simulations of a homogeneous, shallow-water flow in an idealised basin, thus avoiding several factors (vertical stratification, irregular topography, complicated forcing forms) that may obscure or inhibit the cascade towards a 'condensate' state. In the first set of simulations, the flow is initialised with a randomly perturbed condition, slowly decaying due to weakly viscous effects. It will be shown that a clear cyclonic circulation over the topographic slopes is formed around the basin, together with an anticyclonic vortex in the central part. Afterwards, we shall discuss the main features of the resulting flows in terms of the characteristics of the initial conditions. The second set of experiments consists of fluid initially at rest and set in motion by a random forcing until reaching a statistically stationary state. It will be shown that a similar configuration as in the decaying case is found: a cyclonic (anticlockwise) boundary flow over the topography and an anticyclonic circulation at the central part of the basin.

The previous studies that have addressed the two essential results previously described (cyclonic flow around the basin and a central anticyclone in the northern hemisphere) were focused on decaying flows over relatively gentle topographies using a quasi-geostrophic (QG) model [15,18] or a primitive equation model [17]. The QG dynamics are restricted to small topographic changes compared to the total depth. In contrast, we use a shallow-water model, allowing abrupt topographies. With this formulation, we can study steep continental slopes near the basin boundaries [8,26]. In a recent paper, we employed a similar system using small and large-scale forcing functions to analyse their competing effects on a large basin under the β-plane approximation (where the Coriolis parameter varies linearly with the latitude) [20]. We restrict the present study to the f-plane (constant Coriolis parameter), so we will consider the basin horizontal scale of a few hundred kilometres.

In Sec. 2, we present the physical model and the design of the numerical experiments. The results for decaying flows are presented in Sec. 3, and the simulations with random forcing in Sec. 4. Section 5 summarises the conclusions and recommendations for future studies.

2. Methods

2.1. Shallow-water model

Consider an oceanic, homogeneous flow in a square basin with topography in an f-plane with constant Coriolis parameter f_0 (s^{-1}). In a Cartesian coordinate system, the rotation axis is in the vertical direction z. Under the shallow-water (SW) approximation, the flow is sufficiently slow so that it remains in hydrostatic balance [27]. Thus, the horizontal flow field $\mathbf{u} = (u, v)$ is assumed to depend only on the horizontal coordinates (x, y) so that $u \equiv u(x, y, t)$ and $v \equiv (x, y, t)$. Under the rigid-lid approximation, the fluid depth is denoted $h(x, y)$ and moves in vertical columns that might be stretched or squeezed when flowing over troughs or bumps, respectively. The flow is governed by the SW vorticity equation [28]

$$\frac{\partial \omega}{\partial t} + J(q, \psi) = A\nabla^2\omega + D + F, \tag{1}$$

where ω is the vertical component of the relative vorticity, ψ a transport function (with units of volume over time), and q the potential vorticity

$$q = \frac{\omega + f_0}{h}. \tag{2}$$

Operators $J(a, b) = a_x b_y - a_y b_x$ and $\nabla^2 a = a_{xx} + a_{yy}$ are the Jacobian and the horizontal Laplacian (subindexes indicate partial derivatives), respectively, and A is a turbulent viscous coefficient. Finally, D and F are dissipative and forcing functions, which will be discussed later.

The transport function is defined such that

$$u = \frac{1}{h}\frac{\partial \psi}{\partial y}, \qquad v = -\frac{1}{h}\frac{\partial \psi}{\partial x}. \tag{3}$$

Since $\omega = v_x - u_y$, then

$$\omega = -\frac{1}{h}\nabla^2\psi + \frac{1}{h^2}\nabla h \cdot \nabla\psi. \tag{4}$$

Using the horizontal velocity scale U, and the horizontal and vertical length scales, L and H, the dimensionless vorticity equation is

$$Ro\frac{\partial \omega'}{\partial t'} + J'\left(\frac{Ro\omega' + 1}{h'}, \psi'\right) = \frac{Ro}{Re}\nabla'^2\omega' + D' + F', \tag{5}$$

where the Rossby and the Reynolds numbers are

$$Ro = \frac{U}{f_0 L}, \qquad Re = \frac{UL}{\nu}, \tag{6}$$

respectively. For slowly evolving motions ($Ro \ll 1$), weakly dissipative ($Re \gg 1$), and unforced ($D' = F' = 0$) or in statistical equilibrium ($F' \sim -D'$), the vorticity equation is reduced to

$$\mathbf{u}' \cdot \nabla \left(\frac{1}{h'} \right) \approx 0. \tag{7}$$

In such conditions, the fluid tends to follow the (dimensional) geostrophic contours f_0/h (or, equivalently, the topographic contours of h). Such a tendency suggests the generation of cyclonic currents in a closed basin with topography, as discussed in the Introduction.

2.2. Numerical model

2.2.1. *Numerical scheme*

The model Eqs. (1)-(4) are numerically solved with a finite differences scheme. R.Verzicco developed the original code [29], and subsequent versions have been used to study inviscid and viscous topography effects in rotating systems (a comprehensive review is given in Ref. [8]). Forced systems in closed domains have been simulated in Refs. [20,28,30]. The time advancement is performed with an explicit, third-order Runge-Kutta method. An important feature is that the nonlinear terms are spatially discretised with an Arakawa scheme, avoiding the spurious production of energy and enstrophy. The viscous terms are discretised with a centred, second-order, Crank-Nicolson scheme to reduce numerical diffusion. The vorticity-transport function Eq. (4) is inverted with a multigrid method from a NAG routine.

2.2.2. *Ocean basin with topography*

We consider a homogeneous fluid confined in a square basin in a horizontal domain $-L \le x \le L$ and $-L \le y \le L$, with $L = 600$ km. The fluid depth is

$$h(x, y) = H \exp\left(-\frac{|x|^{10} + |y|^{10}}{L_d^{10}} \right). \tag{8}$$

The central part of the basin is nearly flat with a maximum depth of $H = 3000$ m (Fig. 1). Near the walls, the topography consists of steep slopes modulated by the horizontal scale $L_d = 0.98L$. The fluid depth at the walls is $h \sim 0.3H$, and the slope width is about $L/6$, so the slopes are approximately $s \approx 5.1 \times 10^{-3}$. The basin is similar to that used in Ref. [20], but here the size is smaller to restrict the dynamics to the f-plane (with $f_0 = 10^{-4}$ s^{-1}). The topographic effects can be quantified with the topographic β parameter defined as $\beta_t = sf_0/H$ [26]. For the present parameters, $\beta_t \sim 1.7 \times 10^{-10}$ (ms)$^{-1}$.

The square domain is discretised in a rectangular grid with sufficient resolution to solve mesoscale motions (vortical structures with length scales from 10 km to a few hundred km. The main results (instantaneous and long-term averages of the dynamical fields) did not show significant differences when using 257×257 points (resolution of $dx = dy \approx 4.7$ km), or a finer grid of 513×513 points. The effects of submesoscale eddies are represented by a turbulent viscosity coefficient A ranging between 8 and 50 m^2/s. The boundary conditions at the walls are no-slip ($u = v = 0$). The constant time step is $dt = 3600$ s.

Two types of experiments are performed: freely decaying flows by lateral viscous effects and continuously forced turbulence including bottom friction. The duration of the simulations varies between one and five years, depending on the kind of experiment, as explained below.

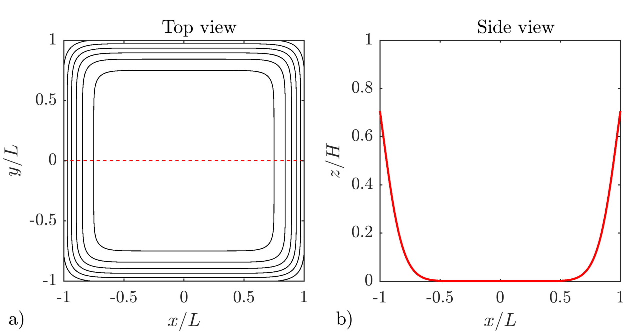

FIGURE 1. Bottom topography. a) Depth contours of the oceanic square basin (8. Outer (inner) contour is 800 m (2800 m); the contour interval is 400 m. b) Normalised topography profile $1 - h(x, 0)/H$ along the red dashed line in a).

2.2.3. *Decaying turbulence*

The experiments of Sec. 3 consist of the slowly viscous decay due to lateral friction of an initially disordered flow. Several methods exist to prescribe an initially random vorticity field for the decaying turbulence experiments. Here, we choose an array of 10×10 circular vortices centred at the square domain. Each vortex has a Gaussian profile

$$\omega_{ij} = \omega_{0ij} \exp(r_{ij}^2/R^2), \tag{9}$$

where $i, j = 1 \dots 10$ numerate the row and column of each vortex in the rectangular coordinates, ω_{ij0} are the peak vorticities, R a common radial scale, and r_{ij} the radial coordinates with origin at each vortex. The absolute value of the peak vorticities is the same for all vortices $|\omega_{0ij})| = \omega_0$ for all i, j. We choose $\omega_0 = 0.25 \times 10^{-5}\,\mathrm{s}^{-1} \ll f_0$ in all simulations to ensure a low Rossby number. The radius of the vortices is $R = L/12$, so there is a stripe of zero vorticity adjacent to the lateral walls.

An advantage of this configuration is that the initial circulation is easily controlled by choosing the number of positive and negative vortices disposed in random positions. Given the vorticity field ω, the total circulation is defined as

$$C(t) = \iint \omega dx dy. \tag{10}$$

For instance, the array in Fig. 2a) contains 50 cyclones and 50 anticyclones, so the initial circulation is zero.

The total energy per mass unit is

$$E(t) = \frac{1}{2V} \iint h(u^2 + v^2) dx dy, \tag{11}$$

where V is the total fluid volume. We calculate an initial velocity scale $U = \sqrt{2E_0}$, with $E_0 \equiv E(0)$, to define the Rossby and Reynolds numbers characterising each experiment. All simulations in Sec. 3 start with the same initial energy E_0 (same U) and such that $Ro = 10^{-3} \ll 1$. The duration of the simulations is one year.

2.2.4. *Continuously forced turbulence*

The simulations of Sec. 4 represent the flow behaviour in the presence of a time-dependent random forcing $F(x, y, t)$ in Eq. (1). In these experiments, the flow starts at rest, and the forcing sets the fluid in motion until reaching a statistically stationary state. To counteract the forcing, we also include bottom friction $D(x, y, t)$ so that the energy injected by the force is mainly balanced with this dissipative effect [31]. The duration of the simulations is five years.

The forcing field F is based on the method designed in Ref. [32] and employed in Ref. [20]. Function F is a sum of nine harmonic modes with different wavelengths, each of them with a random phase that changes every time step. The forcing slowly evolves because it is based on a first-order Markov process with a decorrelation time of three days. Though the forcing modes are anisotropic, they all have a similar wave number magnitude that sets the forcing scale at approximately $L/15 = 40$ km. The forcing function has a given amplitude F_0.

The dissipative term D consists of a linear term representing Ekman bottom friction [33], $D = -(\alpha/h)\omega$, where α is a friction coefficient with typical values of 4×10^{-4} m/s [28,34]. Simulations with different combinations of the forcing amplitude F_0 and friction α were performed, such that the statistical equilibrium states had a different energy level. For further details, see [20]. The highest root-mean-square velocity U_S in a simulation was about 1.2 times the velocity scale U of the decaying experiments. Thus, the Rossby number $Ro = U_S/f_0L$ remained small in all experiments, and the Reynolds numbers were comparable.

3. Simulations of decaying turbulence

The first set of experiments consists of a random initial flow covering the entire flow domain that slowly decays due to lateral viscosity. During decay, the flow energy cascades towards larger scales until a final quasi-steady configuration is reached. Decaying turbulence is examined to appreciate better the process leading to self-organized states. The results vary depending on the initial circulation (10).

3.1. Zero initial circulation, $C = 0$

Figure 2 shows a sequence of four snapshots of the relative vorticity and velocity fields in a typical experiment illustrating the flow evolution during one year. The initial condition in Fig. 2a) is a random array of 10×10 vortices, 50 cyclonic and 50 anticyclonic, so the initial circulation is zero. At subsequent times, the flow is rapidly affected by the topography near and along the sidewalls: the vorticity field is aligned in thin stripes along the topography, and the velocity field depicts a cyclonic circulation around the basin. In contrast, the central region presents the expected self-advection of vortex dipoles and merging of equally-signed vortices typical of 2D

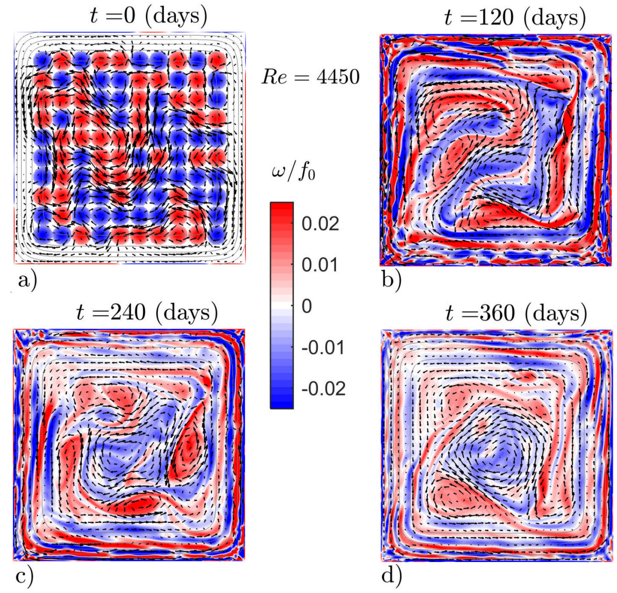

FIGURE 2. Relative vorticity divided by f_0 (colours) and 2D velocity fields (black arrows) at four times during one year in a simulation with $Re = 4450$. The velocity arrows are scaled to become visible as the flow decays. The velocity scale $U(t) = \sqrt{2E(t)}$ at each time is $U(t)/U = [1, 0.82, 0.66, 0.58]$. Grey lines are topography contours (800:40:2800 m).

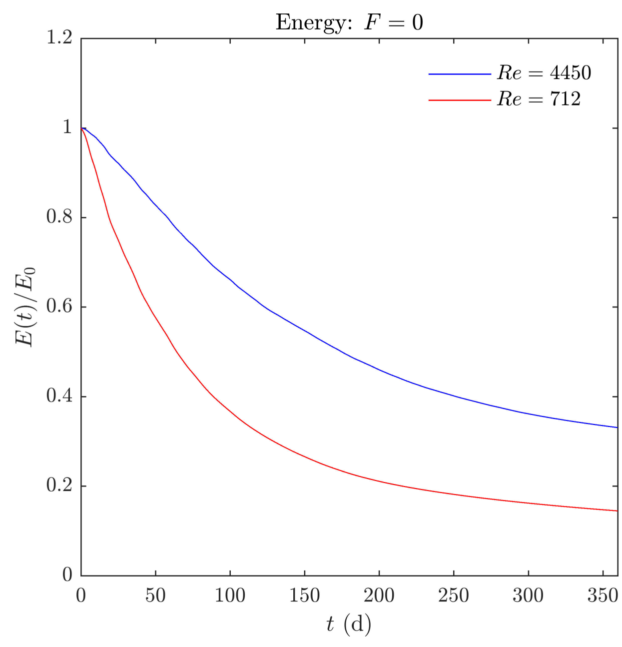

FIGURE 3. Time evolution of the total kinetic energy (11) normalised with the initial value $E_0 = 0.0018$ m^2/s^2 in decaying turbulence simulations with $Re = 4450$ (blue) and $Re = 712$ (red).

turbulence. At later times, these processes cascade the energy towards larger scales and form an anticyclonic structure [Fig. 2d)]. The negative vortex is not perfectly circular: other minor cyclonic structures around the main vortex are still in the flat region. The decay of the total kinetic energy is shown in Fig. 3 together with the corresponding curve in an experiment with a flow having less inertia, $Re = 712$. Of course, the lower the Re, the faster the energy decay.

The described processes were obtained for various initial conditions, Re numbers, similar domains and topographic fields. Though the details might differ, the general result is that the viscous decay of quasi-2D turbulence in the basin consists of (i) a well-defined anticlockwise current along the topography and (ii) the formation of an anticyclonic vortex in the central, flat region. The current around the basin runs with shallow water to the right because $f_0 > 0$ (northern hemisphere). Figure 4 illustrates these results by calculating time averages (denoted with brackets) of the dynamic fields for the previously discussed simulation with $Re = 4450$ and the case with $Re = 712$. The upper panels (a,b) show the time-averaged vorticity fields between days 181 to 360 in both simulations, a period in which the current over the topography and the central anticyclone have been formed. The lower panels present the average velocity field (arrows) and magnitude (colours) averaged in the same period. Some differences are that the anticyclonic vortex in the central region for $Re = 4450$ has a more significant vorticity and velocity magnitude (panels a,c) than the structure with $Re = 712$ (panels b,d). The reason is simply that the second case decays faster.

More detailed differences can be observed in the meridional and zonal velocity profiles averaged in time and space, defined as [20]

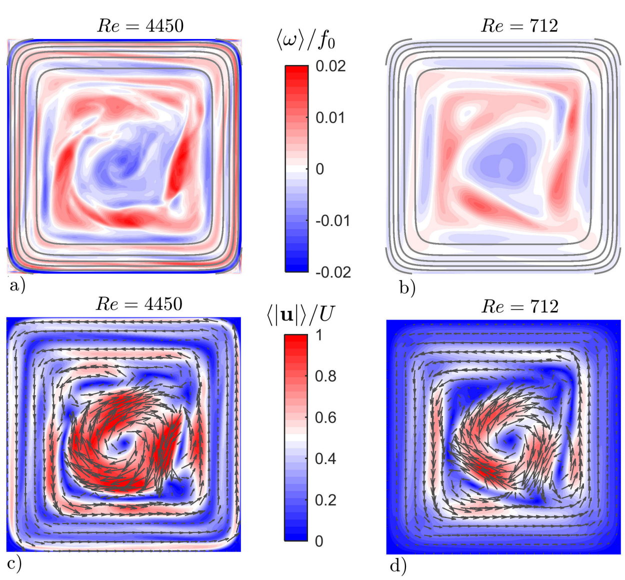

FIGURE 4. Normalised mean relative vorticity a), b) and velocity field c), d) in simulations with $Re = 4450$ and $Re = 712$. The time average is computed with 180 daily fields from day 181 to 360.

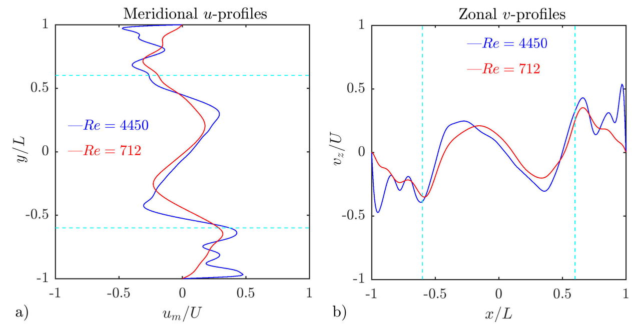

FIGURE 5. Normalised a) meridional u-profiles and b) zonal v-profiles calculated with (12) and (13), respectively, for the simulations in Fig. 4. Dashed lines separate the central part of the domain from the sloping topography regions.

$$u_m(y) = \frac{1}{2L}\int_{-L}^{L} \langle u(x,y)\rangle dx, \tag{12}$$

$$v_z(x) = \frac{1}{2L}\int_{-L}^{L} \langle v(x,y)\rangle dy. \tag{13}$$

Figure 5a) shows the spatio-temporal average of the zonal velocity $u_m(y)$ at different latitudes. Dashed lines separate the boundary regions with the sloping topography and the central area. The profiles denote the anticlockwise circulation over the topography and the anticyclonic flow at the central part. A similar configuration is found in Fig. 5b) for the meridional velocity profiles $v_z(x)$. In general, for lower Re, the average flow is weaker, and the boundary layers are wider. For higher Re, the flow along the topography exhibits finer structures.

3.2. Non-zero initial circulation, $C \neq 0$

The previous results suggest the configuration to which any turbulent flow with zero circulation initially evolves in the basin. However, the results might differ when the initial flow is sufficiently biased to circulate in a pre-established direction. Here, we examine two simulations of decaying turbulence that are initialised with random fields with negative ($C < 0$) and positive ($C > 0$) circulations, as defined in (10). The positive (negative) circulation field has 60 (40) cyclones and 40 (60) anticyclones randomly disposed (the vorticity fields are identical, but one of them is multiplied by minus one, so we obtain the same opposite-sign circulation exactly). The simulations start with the same total energy, so the velocity scale U is the same, and it is chosen identical to the case shown in Fig. 2 with zero circulation.

Figure 6 shows the time-averaged vorticity and velocity fields similarly as in Fig 4. For $C > 0$ [Figs. 6a), c)], the anticlockwise current over the topography is intensified and looks more organised in comparison with the $C = 0$ case [Fig. 4a), 4c)]. Also, the anticyclone in the nearly flat region is formed again, though somewhat smaller. Thus, the initially random field with $C > 0$ enhances the topographically forced

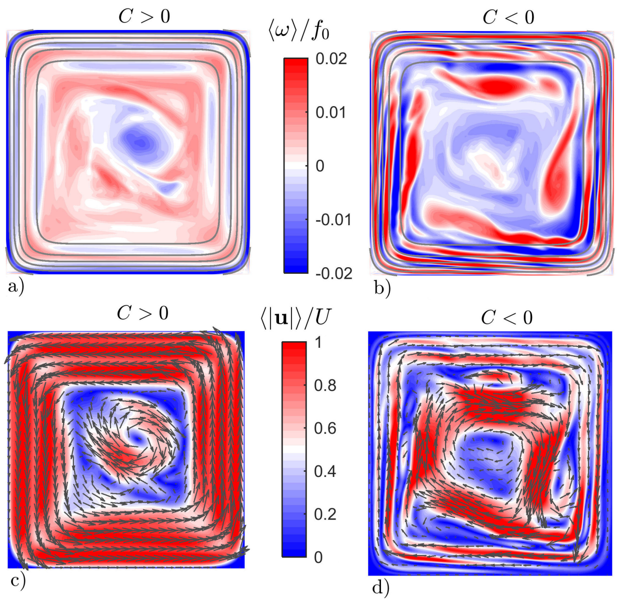

FIGURE 6. Normalised mean relative vorticity a), b) and velocity field c), d) in simulations with initially positive $C > 0$ and negative $C < 0$ circulation ($|C| = 2.055 \times 10^5$ m^2/s). The time average is computed with 180 daily fields from day 181 to 360. In both experiments, the initial energy is the same and the Reynolds number is $Re = 4450$.

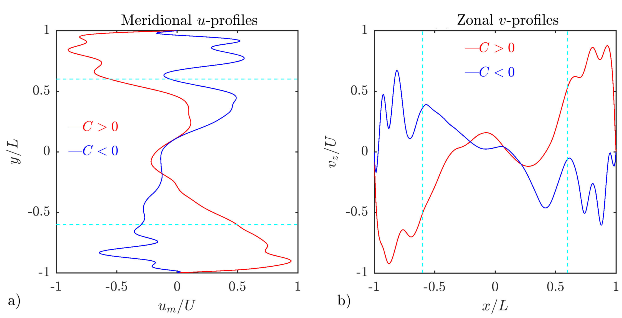

FIGURE 7. Spatio-temporal average velocity profiles as in Fig. 5 but now for the simulations initialised with $C > 0$ and $C < 0$ (see Fig. 6).

current around the basin. The case with $C < 0$ is different [Figs. 6b), 6d)]. The central anticyclone has also been formed but is now much more prominent and practically covers the whole domain, including the boundary region over the topographic slopes. This simulation shows that a sufficiently negative initial circulation might inhibit and even reverse the topographic flow over the topography. Nevertheless, the anticyclone at the central region is always formed.

To better appreciate the central anticyclone and the boundary current over the topography, Fig. 7 presents the meridional and zonal velocity profiles calculated from both experiments. Regarding the circulations over the slopes, the anticlockwise flow for $C > 0$ (red curves) is more intense than the clockwise motion found for $C < 0$ (blue curves). The anticyclonic profiles at the central area in the $C < 0$ experiment are more intense and broader than those in the $C > 0$ case.

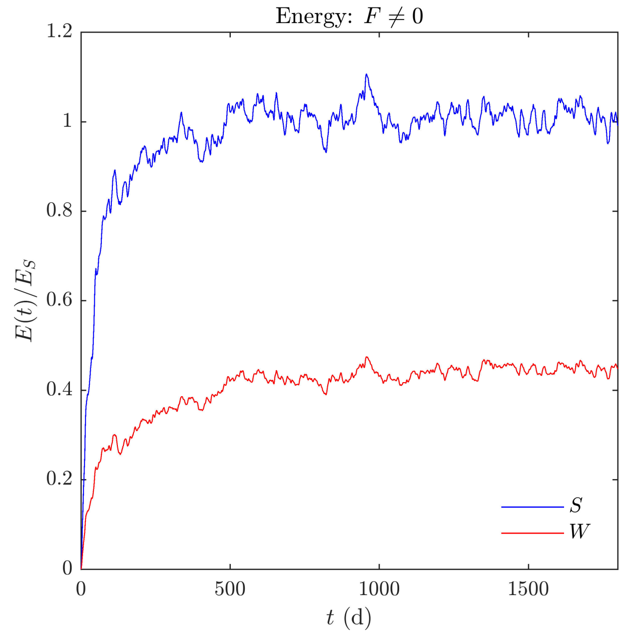

FIGURE 8. Time evolution of the total kinetic energy (11) in continuously-forced turbulence simulations with ‘strong’ (S, blue) and ’weak’ (W, red) forcing. Both curves are normalised with the equilibrium energy $E_S = 0.002$ m^2/s^2 in simulation S, calculated with 1620 daily velocity fields from day 181 to 1800.

4. Randomly forced turbulence

In this section, we study the flow behaviour in the presence of a time-dependent random forcing over the whole domain. The continuously forced flows are analysed to demonstrate that even in the presence of a time-dependent random forcing, the flow evolves towards a preferred state determined by the topography. The forced case is also interesting because actual oceans are usually subject to continuous forcing from different sources, especially the wind.

The flow starts at rest, and the forcing sets the fluid in motion until it reaches a statistically steady state. To counteract the forcing, we also include bottom friction so the energy injected by the forcing is balanced with dissipative effects (see Sec. 2). The duration of the simulations is five years. Figure 8 shows the time evolution of the total energy in two typical experiments, one of them with ‘strong’ forcing (S) and the other ‘weaker’ (W). The quasi-steady state is approximately reached after 500 days in both cases. After that, the energy is nearly constant. The total energy E_S in simulation S is slightly more than two times the energy in W. A close inspection reveals that the two series are correlated because the spatial and temporal variation of the forcing is the same, but the amplitude is different. A different forcing protocol gives similar results (not shown).

Now, we examine to what extent the results found for decaying flows occur again in the presence of continuous forcing. Figures 9a), 9b) present two snapshots of the relative vorticity at days 720 and 1080 (years 2 and 3, approximately)

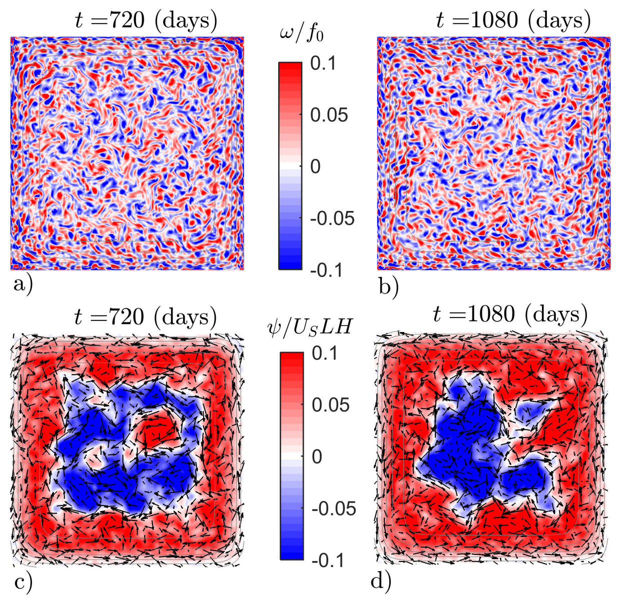

FIGURE 9. a), b): Relative vorticity divided by f_0 (colours) at two times (720 and 1080 days) in simulation S. c), d) Transport function (colours) and 2D velocity fields (black arrows) at the same days. The velocity scale based on the equilibrium energy is $U_S(t) = \sqrt{2E_S(t)} = 0.06$ m/s.

in simulation S. The vorticity fields illustrate that the instantaneous flow state shows no apparent order. In particular, the central region remains highly turbulent during the whole simulation. However, an anticlockwise current along the topography that remains very close to the walls can be observed in animated daily sequences (a similar result was reported in the supplementary movies of [20]). The corresponding transport function and velocity fields are shown in Figs. 9c), 9d). The velocity arrows look very disordered, even near the walls, but the transport function shows a somewhat clearer configuration, with positive values over the topography and negative circulation over the flat region. This arrangement roughly remains consistent at both times. Similar results are found in simulation W (not shown). In summary, the randomly forced flow exhibits a disordered state throughout the simulation, although the transport function suggests some order that persists at different times.

To detect the equilibrium state more clearly, we have to calculate average fields. Figure 10 presents the average transport function and the velocity field in the simulations S and W. In this case, it is more convenient to present the ψ fields instead of ω because the vorticity fields are very noisy due to the random forcing. Remarkably, the two main results observed for decaying flows are found again in the mean fields of the forced simulations: a well-defined anticlockwise current is established over the coastal slopes, and an anticyclonic flow is developed at the central region of the basin. Of course, the structure of both features is very different from the decaying examples. The boundary current is more irregular, as is the central anticyclone. Also, the maximum values of the two structures are located differently than those of the decaying experiments.

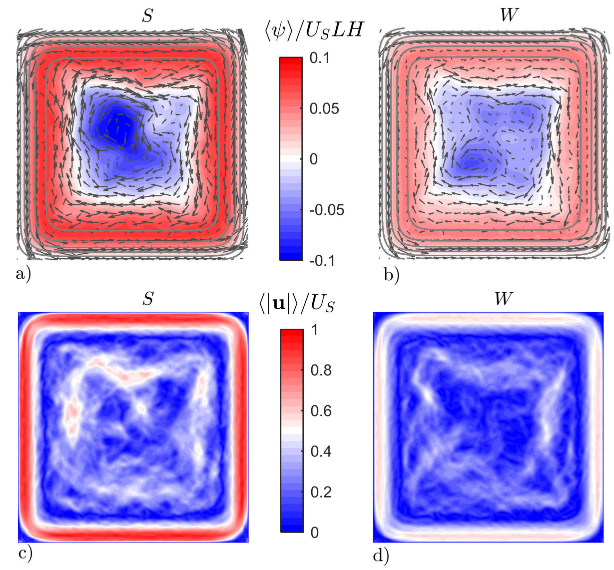

FIGURE 10. Normalised mean transport function a), b) and velocity field c), d) in continuously-forced simulations with strong S and weak W forcing. The time average is computed with 1620 daily fields from day 181 to 1800. The ψ fields are normalised with the velocity scale $U_S = \sqrt{2E_S}$ in simulation S, the half-length of the domain L and the maximum depth H.

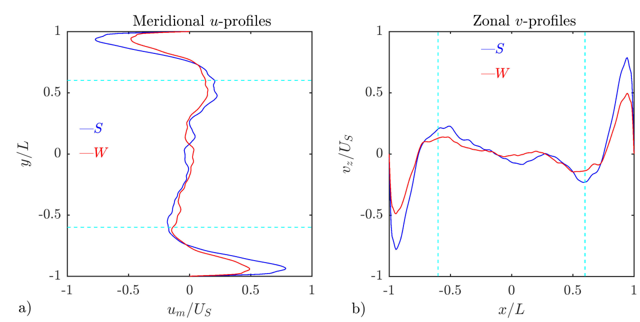

FIGURE 11. Spatio-temporal average velocity profiles as in Fig. 5 but now for the continuously-forced simulations with strong (S) and weak (W) forcing (see Fig. 10).

To emphasise the previous results, Fig. 11 shows the average meridional and zonal velocity profiles. These profiles can be compared, again, with the results for decaying turbulence in Figs. 5 and 7. Note that the anticlockwise flow along the topography remains very close to the solid walls and is relatively thin. The profiles at the central region denote the anticyclonic gyre. Recall that these results are obtained (in average) even in the presence of the random forcing.

5. Discussion and conclusions

We studied the evolution of oceanic-scale turbulent flows in a closed basin with sloping topography adjacent to the side walls. The analyses were focused on (i) decaying turbulence from an initially random state and (ii) continuously forced turbulence starting from rest and reaching a quasi-stationary state. The two most important results are (1) the formation of a steady, anticlockwise flow around the basin and along the topography contours (for a positive Coriolis parameter or northern hemisphere), and (2) the spontaneous generation of an anticyclonic vortex at the nearly-flat central part of the domain. It can be said that such a state is the 'preferred' configuration to which the turbulence of a weakly viscous flow evolves in this system.

The formation of a current over the topography having shallow water to the right is expected from previous theories related to the statistical equilibrium state of the system [9,10,21]. The systematic formation of an anticyclone in the central part must be related to the inverse energy cascade over a flat region, which implies condensation into one or two single vortices of aleatory sign [5,35]. However, it needs to be clarified why the surrounding topography influences the central region in producing an anticyclone in almost all cases.

The main results were found for arbitrary initial conditions with zero and positive circulation for decaying flows. However, when the initial circulation is sufficiently negative, the resulting configuration tends to be anticyclonic over the whole domain, including the coastal areas with topography. Thus, the initial condition might influence the long-term evolution. Regarding the continuously forced flows, it is remarkable that the flow tends to the preferred configuration even when the forcing is entirely random in time and space with no preferential forcing in any direction.

The present experiments are highly idealised and can be improved in several ways. We enumerate some of them here, though there can be many more.

1. The bottom topography strongly influences the barotropic flow because the fluid parcels are vertical columns that are squeezed or stretched when moving down or upslope. Such an influence might be different in a stratified system. Thus, the effects of stratification should be considered in more elaborate models. The most straightforward approach is the barotropic-equivalent model, which assumes a vertical structure of the fluid layer [28]. Fully baroclinic models should also be used, as has been recently explored in Refs. [17,18].

2. The present discussion is restricted to the f-plane dynamics, so the results might sensibly change for larger basins on the β-plane, where the Coriolis parameter varies with latitude. In those cases, the continuous competition between the planetary and the topographic β effects might lead to different flow configurations. Randomly forced flows in a similar square basin on a β-plane were examined in Ref. [20], where the results suggested the average formation of an anticyclonic cell shifted to the southward part of the basin.

3. We found that the circulation sign of the initial condition in the decaying experiments influences the long-term state. This result should be studied further to determine the pre-existing conditions that lead to the preferred state.

4. The same argument applies to the type of forcing in the continuously forced experiments. We found that the random forcing leads to the expected configuration. However, what happens when the forcing is not aleatory but imprints a preferred circulation on the flow? The chosen forcing is expected to reinforce or counteract the formation of the central anticyclone and the coastal current, as discussed in Ref. [20].

5. Another essential issue is to study more complicated shapes of the basin and different bottom topography parameters. For instance, the competition between the topographic β-effect and the flow inertia in a topographic depression with no lateral walls was studied in Ref. [17]. A sufficiently strong topographic β-effect inhibits the vortex propagation and promotes that the formed anticyclones remain over the depression.

The main results described above give new insights into the formation of cyclones and anticyclones in oceanic basins. In particular, the results provide arguments for the formation of anticyclones in the Lofoten basin and other locations in the northern hemisphere [18] and with physical extensions comparable to those used here. The persistent anticyclones observed there may be partially a consequence of the quasi-2D, inverse energy cascade influenced by the shape of the basin.

However, if the average wind blowing over an oceanic basin has a dominant positive or negative curl, then this preferential forcing may trigger the formation of cyclones or intensified anticyclones. Under this argument, the regular occurrence of the large Campeche cyclone in the southwestern side of the Gulf of Mexico might be formed by the persistent positive wind curl present most of the year [24,36]. We conclude that the formation of cyclones or anticyclones over topographic depressions and basins in the ocean should be further investigated in light of the turbulent theory of topographically forced flows.

1. R. H. Kraichnan, Inertial ranges in two-dimensional turbulence, *The Phys. Fluids* **10** (1967) 1417, `https://doi.org/10.1063/1.1762301`.

2. G. Boffetta and R. E. Ecke, Two-dimensional turbulence, Ann. *Rev. Fluid Mech.* **44** (2012) 427, `https://doi.org/10.1146/annurev-fluid-120710-101240`.

3. H. J. H. Clercx and G. J. F. van Heijst, Two-dimensional Navier-Stokes turbulence in bounded domains, *Appl. Mech. Rev.* **62** (2009) 020802, `https://doi.org/10.1115/1.3077489`.

4. S. D. Danilov and D. Gurarie, Quasi-two-dimensional turbulence, *Physics-Uspekhi* **43** (2000) 863, https://doi.org/10.1070/PU2000v043n09ABEH000782.
5. G. J. F. van Heijst and H. J. H. Clercx, Studies on quasi-2D turbulence- the effect of boundaries, *Fluid Dyn. Res.* **41** (2009) 064002, https://doi.org/10.1088/0169-5983/41/6/064002.
6. G. I. Taylor, Experiments with rotating fluids, *Proc. R. Soc. Lond. A* **100** (1921) 114, https://doi.org/10.1098/rspa.1921.0075.
7. G. J. F. van Heijst and H. J. H. Clercx, Laboratory modeling of geophysical vortices, *Annu. Rev. Fluid Mech.* **41** (2009) 143, https://doi.org/10.1146/annurev.fluid.010908.165207.
8. L. Zavala Sansón and G. van Heijst, Laboratory experiments on flows over bottom topography, Modeling Atmospheric and Oceanic Flows: Insights from Laboratory Experiments and Numerical Simulations, edited by T. von Larcher and P. D. Williams (Wiley, New York) (2014). https://doi.org/10.1002/9781118856024.ch7.
9. R. Salmon, Lectures on Geophysical Fluid Dynamics (Oxford University Press, 1998).
10. F. P. Bretherton and D. B. Haidvogel, Two-dimensional turbulence above topography, *J. Fluid Mech*. **78** (1976) 129, https://doi.org/10.1017/S002211207600236X.
11. W. J. Merryfield, P. F. Cummins, and G. Holloway, Equilibrium statistical mechanics of barotropic flow over finite topography, *J. Phys. Oceanogr.* **31** (2001) 1880, https://doi.org/10.1175/1520-0485(2001)031%3C1880:ESMOBF%3E2.0.CO;2.
12. L. Zavala Sansón, A. González-Villanueva, and L. M. Flores, Evolution and decay of a rotating flow over random topography, *J. Fluid Mech.* **642** (2010) 159, https://doi.org/10.1017/S0022112009991777.
13. M. Tenreiro *et al*., Experiments and simulations on selforganization of confined quasi-two-dimensional turbulent flows with discontinuous topography, *Phys. Fluids* **22** (2010) 02511, https://doi.org/10.1063/1.3313928.
14. L. Zavala Sansón, A. C. B. Aguiar, and G. J. F. van Heijst, Horizontal and vertical motions of barotropic vortices over a submarine mountain, *J. Fluid Mech.* **695** (2012) 173, https://doi.org/10.1017/jfm.2012.9.
15. P. F. Cummins and G. Holloway, On eddy-topographic stress representation, *J. Phys. Oceanogr.* **24** (1994) 700, https://doi.org/10.1175/1520-0485(1994)024%3C0700:OESR%3E2.0.CO;2.
16. J. Wang and G. K. Vallis, Emergence of Fofonoff states in inviscid and viscous ocean circulation models, *J. Mar. Res.* **52** (1994) 83, https://elischolar.library.yale.edu/journalofmarineresearch/2089.
17. A. Solodoch, A. L. Stewart, and J. C. McWilliams, Formation of anticyclones above topographic depressions, *J. Phys. Oceanogr*. **51** (2021) 207, https://doi.org/10.1175/JPO-D-20-0150.1.
18. J. H. LaCasce, A. Palóczy, and M. Trodahl, Vortices over bathymetry, *J. Fluid Mech*. **979** (2024) A32, https://doi.org/10.1017/jfm.2023.1084.
19. A. Roubicek, E. Chassignet, and A. Griffa, Topographic stress parameterization in a primitive equation ocean model: Impact on mid-latitude jet separation, In Flow-Topography, Proceedings of Aha Hliko'a Hawaiian Winter Workshop, University of Hawaii (1995) pp. 239-252.
20. L. Zavala Sansón, Effects of mesoscale turbulence on the wind-driven circulation in a closed basin with topography, *Geophys. Astrophys. Fluid Dyn*. **116** (2022) 159, https://doi.org/10.1080/03091929.2022.2065271.
21. G. Holloway, Representing topographic stress for large-scale ocean models, *J. Phys. Oceanogr.* **22** (1992) 1033, https://doi.org/10.1175/1520-0485(1992)022%3C1033:RTSFLS%3E2.0.CO;2.
22. G. Holloway, Observing global ocean topostrophy, *J. Geophys. Res. Oceans* **113** (2008) C7, https://doi.org/10.1029/2007JC004635.
23. A. M. Vázquez De La Cerda *et al*., Bay of Campeche circulation: An update, *Goephys. Monogr. AGU* **161** (2005) 279, https://doi.org/10.1029/161GM20.
24. L. Zavala Sansón, J. Sheinbaum, and P. Pérez-Brunius, Single-particle statistics in the southern Gulf of Mexico, *Geofís. Int.* **57** (2018) 139.
25. M. Trodahl *et al*., The regeneration of the Lofoten Vortex through vertical alignment, *J. Phys. Oceanogr*. **50** (2020) 2689, https://doi.org/10.1175/JPOD-20-0029.1.
26. L. Zavala Sansón and G. J. F. van Heijst, Interaction of barotropic vortices with coastal topography: Laboratory experiments and numerical simulations, *J. Phys. Oceanogr*. **30** (2000) 2141, https://doi.org/10.1175/1520-0485(2000)030%3C2141:IOBVWC%3E2.0.CO;2.
27. J. Pedlosky, Geophysical fluid dynamics (Springer Science & Business Media, 1987).
28. L. Zavala Sansón, Nonlinear and time-dependent equivalent-barotropic flows, *J. Fluid Mech.* **871** (2019) 925, https://doi.org/10.1017/jfm.2019.354.
29. R. Verzicco *et al.*, Numerical and experimental study of the interaction between a vortex dipole and a circular cylinder, *Exp. Fluids* **18** (1995) 153, https://doi.org/10.1007/BF00230259.
30. A. S. González Vera and L. Zavala Sansón, The evolution of a continuously forced shear flow in a closed rectangular domain, *Phys. Fluids* **27** (2015) 034106, https://doi.org/10.1063/1.4915300.
31. R. K. Scott and D. G. Dritschel, The structure of zonal jets in geostrophic turbulence, *J. Fluid Mech*. **711** (2012) 576, https://doi.org/10.1017/jfm.2012.410.
32. D. K. Lilly, Numerical simulation of two-dimensional turbulence, *Phys. Fluids* **12** (1969) II, https://doi.org/10.1063/1.1692444.
33. L. Zavala Sansón and G. J. F. van Heijst, Ekman effects in a rotating flow over bottom topography, *J. Fluid Mech.* **471** (2002) 239, https://doi.org/10.1017/S0022112002002239.

34. J. H. LaCasce and P. E. Isachsen, The linear models of the ACC, *Progr. Oceanogr.* **84** (2010) 139, https://doi.org/10.1016/j.pocean.2009.11.002.

35. S. Maassen, H. Clercx, and G. van Heijst, Self-organization of quasi-two-dimensional turbulence in stratified fluids in square and circular containers, *Phys. Fluids* **14** (2002) 2150, https://doi.org/10.1063/1.1480263.

36. G. Gutiérrez de Velasco and C. D. Winant, Seasonal patterns of wind stress and wind stress curl over the Gulf of Mexico, *J. Geophys. Res. Oceans* **101** (1996) 18127, https://doi.org/10.1029/96JC01442.